Enhanced visible light photocatalytic hydrogen evolution via cubic CeO$_2$ hybridized g-C$_3$N$_4$ composite

Weixin Zou [a,b], Ye Shao [a,b], Yu Pu [a,b], Yidan Luo [a,b], Jingfang Sun [a,b], Kaili Ma [a,b], Changjin Tang [a,b,*], Fei Gao [a,b], Lin Dong [a,b,*]

[a] Key Laboratory of Mesoscopic Chemistry of MOE, School of Chemistry and Chemical Engineering, Nanjing University, Nanjing 210093, PR China
[b] Jiangsu Key Laboratory of Vehicle Emissions Control, Center of Modern Analysis, Nanjing University, Nanjing 210093, PR China

ARTICLE INFO

ABSTRACT

In this work, CeO$_2$ nanocubes hybridized g-C$_3$N$_4$ composites had been facilely synthesized to investigate the interfacial effects on photocatalytic water splitting. The c-CeO$_2$/g-C$_3$N$_4$ composites exhibited the superior photocatalytic hydrogen evolution under visible light irradiation. The optimal c-CeO$_2$ loading content was 5 wt%, with the H$_2$ evolution of 4300 μmol g^{-1} for 5 h illumination, higher than that of pristine CeO$_2$, g-C$_3$N$_4$ and irregular CeO$_2$ nanoparticles/g-C$_3$N$_4$. Moreover, UV–vis DRS, PL spectra and photoelectrochemical measurements demonstrated that 5 wt% c-CeO$_2$/g-C$_3$N$_4$ composite possessed more visible light adsorption and faster charge transfer, which was attributed to the stronger interfacial effects through the presence of the hydrogen bond and p-π hybrid between c-CeO$_2$ {100} and g-C$_3$N$_4$, revealed by the FT-IR and XPS results. The work suggested that engineering the structures of the CeO$_2$ and g-C$_3$N$_4$ interface could be an effective strategy to obtain excellent photocatalysts.

© 2017 Elsevier B.V. All rights reserved.

1. Introduction

With the increased global energy demands and diminishing petroleum reserves, the development of sustainable and clean energy become one of the most significant emergent research fields [1–3]. Hydrogen (H$_2$) energy, considered as an ideal candidate, is received much attention for its environmental friendliness, recycling possibility and high-energy capacity [4,5]. Since 1972, photocatalytic water splitting has been proposed as a promising and attractive approach to get hydrogen energy [6]. Up to now, a large number of photocatalytic materials, with the enhanced band structures, visible light adsorption, charge separation and transport, are designed and developed [7–9].

In recent years, graphitic carbon nitride (g-C$_3$N$_4$) has been regarded as a potential visible light photocatalyst for hydrogen production, since the pioneering work reported by Wang et al. in 2009 [10], due to its advantages of the narrow band gap, excellent stability and fast charge transfer [11–13]. However, the shortcomings are obvious, such as a lack of visible light absorption ($\lambda > 460$ nm), a relatively high recombination of photoinduced charge carriers, a

low specific surface area, etc., which could have a negative effect on the photocatalytic performance [14,15]. Therefore, much effort has been dedicated to the development of highly efficient g-C$_3$N$_4$-based photocatalysts, among which, the construction of hybridized photocatalysts is a widely used route, such as graphene/g-C$_3$N$_4$ [16], CaIn$_2$S$_4$/g-C$_3$N$_4$ [17], ZnO/g-C$_3$N$_4$ [18], etc. These obtained g-C$_3$N$_4$-based composites exhibit superior photocatalytic performances than that of the pure g-C$_3$N$_4$, which could be attributed to the closely contacted interface and well matched band structures between two components, and thus both the separation of photoexcited charges and the photocatalytic process are efficiently promoted. On the basis of that, for hybrid (or composite) catalysts, the interface at which synergistic effect takes place is a crucial point and deserve in-depth exploration [19,20].

Ceria (CeO$_2$), as one of the popular rare earth oxides, is widely used in various fields (such as three-way catalytic converters, fuel cells, water−gas shift reactions, oxygen sensors), due to its abundant redox chemistry, versatile acid and base properties, and high oxygen storage capability [21–24]. Recent researches have found that CeO$_2$ is also an excellent photocatalyst with the feature of narrow band gap, which is able to absorb visible light. In addition, the crystal planes of CeO$_2$ play an important role in photocatalysis [25,26]. It was reported that more oxygen vacancies and adsorption hydroxyl groups were beneficial on CeO$_2$ {100} plane, not {111} plane [27,28]. And the migration abilities of electrons and holes

on {100} and {111} facets are different, holes were encouraged to move toward CeO_2 {100} plane, whereas electrons transferred toward {111} plane, which resulted in various CH_4 evolutions in phototocatalytic reduction of CO_2 [25]. Encouraged by the advantages of CeO_2, a number of CeO_2-based materials (CeO_2-graphene, Au/CeO_2, CeO_2/g-C_3N_4, *etc.*) have been explored for their applications in photodegradation of organic contamination, photocatalytic water splitting and CO_2 reduction [29–31], among which, CeO_2/g-C_3N_4 material had attracted much attention [31–34], researchers employed a lot of characterizations to show that the interfacial interactions were of great significance in separation and transfer of photoexcited charge carriers of CeO_2/g-C_3N_4 catalyst. However, the study on description about the interface interaction between CeO_2 and g-C_3N_4 was rarely reported.

On the basis of the above concepts and ideas, in this work, the cubic CeO_2 {100} hybridized g-C_3N_4 composite with different ratios (donated as cCNx) were designed and prepared to investigate the influence of interfacial effects on the photocatalytic H_2 evolution. It was found that the optimal c-CeO_2 loading content was 5 wt%, exhibiting higher H_2 evolution than that of pristine g-C_3N_4 and CeO_2 nanoparticles/g-C_3N_4, due to more visible light adsorption and faster charge transfer, confirmed by UV–vis DRS, photoluminescence spectra, photoelectrochemical measurements. FT-IR and XPS results showed that the interface of 5 wt% c-CeO_2 {100}/g-C_3N_4 was remarkable, which was from the intensive effects of the hydrogen bond and p-π hybrid on its interface. The schematic illustration of possible interface between c-CeO_2 {100} and g-C_3N_4, as well as, the diagram of electron–hole pair separation and the reaction mechanism were proposed.

2. Experimental section

2.1. Catalyst preparation

Cubic CeO_2/g-C_3N_4 composites were synthesized via a two-step self-assembly procedure, according to the literature [35]. Herein, the g-C_3N_4 support was obtained by the calcination of urea in air at 550 °C for 4 h. The as-prepared g-C_3N_4 was grounded into fine powder, adding to 50 mL methanol with the ultrasonic treatment for 30 min. Subsequently, the prepared cubic CeO_2 suspension prepared by the report [28] was dispersed in 50 mL methanol, which was added to the above g-C_3N_4 under ultrasound for 30 min. Finally, the mixture was stirred in a fume hood for 24 h, in order to remove methanol. The obtained yellow solid was collected, grounded and calcined in a muffle furnace at 100 °C for 4 h. The nominal weight ratios of cubic CeO_2 to g-C_3N_4 were 0, 1, 5 and 7 wt%, and the prepared samples were donated as CN, cCN1, cCN5, and cCN7, respectively.

The preparation of CeCN5 sample was as followed. Firstly, the irregular CeO_2 nanoparticles were obtained by the thermal decomposition of $Ce(NO_3)_3 \cdot 6H_2O$ at 550 °C for 4 h in flowing air. Secondly, the prepared irregular CeO_2 nanoparticles (0.01 g) were added in 50 mL methanol under ultrasound for 30 min. Subsequently, 0.2 g g-C_3N_4 calcinated by urea in air at 550 °C for 4 h was dispersed in 50 mL methanol. Finally, the above CeO_2 suspension dropped into the g-C_3N_4 mixture, and then stirred in a fume hood for 24 h, in order to remove methanol. The obtained yellow solid was collected, grounded and calcined in a muffle furnace at 100 °C for 4 h.

2.2. Catalyst characterization

Scanning electron microscopy (SEM) experiment was performed on a Philips XL30 electron microscope operated at beam energy of 10.0 kV. Transmission electron microscopy (TEM) image was taken on JEM-2100 instrument at an acceleration voltage

of 200 kV. The samples were crushed and dispersed in ethanol and the resulting suspensions were dried on carbon film supported on copper grids. The crystal structures of c-CeO_2/g-C_3N_4 nanocomposites were identified by X-ray diffraction (XRD) with Philips X'Pert Pro diffractometer by Ni-filtered Cu Kα radiation (λ = 0.15418 nm). The X-ray tube was operated at 40 mA and 40 kV. X-ray photoelectron spectroscopy (XPS) analysis was performed on PHI 5000 VersaProbe high performance electron spectrometer, via monochromatic Al Kα radiation (1486.6 eV), the samples were outgassed at room temperature in a UHV chamber ($<5 \times 10^{-7}$ Pa). The sample charging effect was compensated by all binding energies (BE) referenced to 284.6 eV of the C 1s peak. This reference provided BE values with an error within ±0.1 eV. Brunauer–Emmet–Teller (BET) surface area was measured by nitrogen adsorption at 77 K on Micrometrics ASAP-2020 adsorption apparatus. Before each adsorption measurement, approximate 0.1 g catalyst was degassed in the N_2/He mixture at 200 °C for 3 h. The FT-IR spectra were collected from 400 to 4000 cm^{-1} at the spectral resolution of 4 cm^{-1} on Nicolet 5700 FT-IR spectrometer. UV–vis diffuse reflectance spectroscopy (UV-vis DRS) were recorded in the range of 200–800 nm by a Shimadzu UV-2401 spectrophotometer with the reference of $BaSO_4$. Photoluminescence (PL) spectra were determined on a FluroMax-4 fluorescence spectrophotometer. The wavelength of the excitation light was 320 nm. The electron spin resonance (ESR) signal of radicals trapped by 5,5′-dimethyl-1-pirroline-N-oxide (DMPO) reagent was examined on Bruker model ESR JES FA200 (JEOL) spectrometer. The superoxide radicals were obtained at 77 K under visible light.

2.3. Electrochemical measurements

Electrochemical measurements were measured on a CHI660E electrochemical workstation with a standard three-electrode cell. The as-prepared photocatalysts were deposited on fluorine-doped Tin Oxide (FTO) used as a working electrode, while the counter and reference electrodes were a platinum wire and Hg/Hg_2Cl_2 (in saturated KCl) electrode, respectively. The 0.1 M Na_2SO_4 was employed as electrolyte solution. Irradiation was performed by a Xe arc lamp. The working electrodes were prepared as followed: 0.25 g the photocatalyst was grinded with the mixture of 0.5 mL ethanol and 0.06 g polyethylene glycol (PEG, Mw = 20 000), and then the slurry was coated onto a 2 cm × 1 cm FTO glass electrode. Next, these working electrodes were dried in an oven at 100 °C for 10 h.

2.4. Catalytic performances measurement

The photocatalytic hydrogen evolution reaction was carried out in a top-irradiation vessel connected to a gas-closed glass system under an irradiation of 300 W Xe lamp with the 420 nm cut-off filter. 50 mg catalyst was dispersed in 100 mL aqueous solution (90 mL deionized water and 10 mL triethanolamine). H_2PtCl_6 aqueous solution was added which was in-situ reduced to Pt during the reaction (3 wt% Pt). The temperature of solution was kept around 6 °C. The reaction system was sealed and evacuated for 30 min before illumination. The amount of generated hydrogen was determined by a gas chromatograph.

The operation of recycle experiment was as followed: 50 mg catalyst was dispersed in 100 mL aqueous solution (90 mL deionized water and 10 mL triethanolamine). H_2PtCl_6 aqueous solution was added which was in-situ reduced to Pt during the reaction (3 wt% Pt). The temperature of solution was kept around 6 °C. Subsequently, the system was vacuumed before irradiation to remove dissolved air. A 300 W Xe lamp with 420 nm cut-off filter was employed to irradiate the suspension. Every cycle was carried out for 5 h, and at the beginning of every cycle, 10 mL triethanolamine

Table 1
Physicochemical properties of the obtained cCN composites and CN.

Sample	CN	cCN1	cCN5	cCN7	CeO$_2$
Pore size (nm)[a]	35	32	18	28	–
BET surface area (m^2/g)	122	77	81	85	–
Band gap (eV)	2.90	2.85	2.83	2.89	2.50
Decay (ns)[b]	2.60	2.70	2.77	2.64	–
Ce^{3+}/Ce^{4+} (a.u.)[c]	/	0.05	0.23	0.19	–

[a] BJH average pore size.
[b] Based on time-resolved PL spectra.
[c] Calculated from the XPS spectra of Ce 3d.

was added into the reactor. During the interruption of each cycle, the system was vacuumed for 30 min.

3. Results and discussion

3.1. Morphological, structural and photoelectrochemical characterizations

The phase structures of as-prepared c-CeO$_2$/g-C$_3$N$_4$ (cCN) composites and g-C$_3$N$_4$ (CN) were characterized by XRD. In Fig. S1 (in supporting information), the cCN composites and CN showed the typical diffraction peaks at 13.1° and 27.3° of g-C$_3$N$_4$, perfectly indexed as the (100) and (002) planes, respectively, which were ascribed to in-plane structure packing unit and the interlayer stacking [36]. With the increase in the content of CeO$_2$ nanocubes, the intensity of the diffraction peaks at *ca.* 28.5°, 33.1° and 47.4° were gradually obvious, which were attributed to the (111), (200), and (220) crystal planes of the CeO$_2$ (JCPDS no: 04-0802), respectively.

The morphologies of as-synthesized cCN composites were investigated by TEM. As shown in Fig. 1a–d, the ultrafine CeO$_2$, with the cubic structure and the size of *ca.* 20 nm, were successfully anchored onto the g-C$_3$N$_4$ sheets. The HRTEM image was shown in Fig. 1e, corresponding to the yellow framed area in Fig. 1c. From the enlarged high resolution TEM (Fig. 1f), it could be easily observed that the exposed crystal planes of the obtained CeO$_2$ were the (200) planes with the lattice fringes with a spacing of 0.27 nm. With the increased content of CeO$_2$ nanocubes, the aggregation of CeO$_2$ was more serious in cCN7, leading to the grown size. This phenomenon was further observed in SEM-mapping results (Fig. S2). The Ce dispersion of cCN7 composite was more terrible than that of the other cCN composites, which could block the interfacial effect. Based on the XRD, TEM and HRTEM analyses, it was concluded that the cCN composites were formed by the coupling of c-CeO$_2$ {100} crystal planes and g-C$_3$N$_4$ sheets.

For further investigating the effects of CeO$_2$ loading on the pore structure and BET surface areas of as-prepared cCN composites, the nitrogen adsorption/desorption isotherms and pore size distributions of cCN composites and CN were shown in Fig. S3. It was clearly that cCN composites and CN had isotherms of type IV from Brunauer–Deming–Deming–Teller (BDDT) classification, suggesting the presence of mesopores (2–50 nm). The hysteresis loops were attributed to H3 type in a high relative pressure range (0.75 < P/P$_0$ < 1.0), indicating the existence of slit-like pores [27]. Obviously, the pore size distributions of cCN composites and CN were different. The cCN5 had a narrower average pore size (~18 nm) than that of other cCN composites (Table 1). Based on TEM and SEM-EDX results, it was speculated that the dispersion of CeO$_2$ played an important role in the average pore size. The pore size of cCN5 was smaller, for its better dispersion of CeO$_2$. In addition, the BET surface areas were summarized in Table 1. It could be found that cCN composites had the similar BET surface areas, less than that of CN sample.
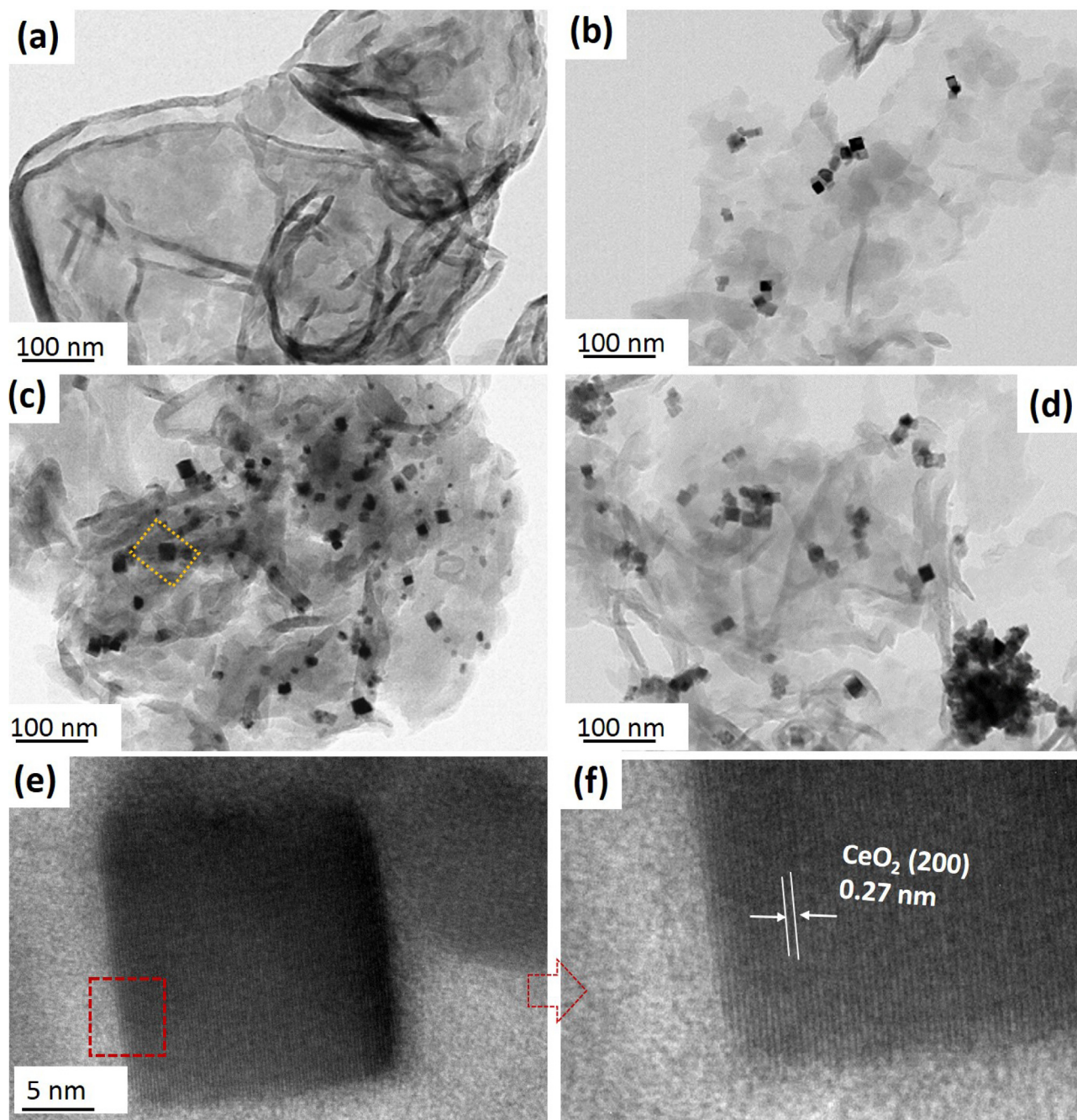
Generally, the optical property was of great significance in photocatalysis. Therefore, the optical absorption properties of cCN composites and CN were investigated in comparison. As shown in Fig. 2a, the absorption edges of the various cCN composites displayed a slight red-shift compared to the CN. The band gap energy of cCN composites was calculated from the formula $(\alpha h\nu)^n = k(h\nu\text{-Eg})$, where α, k, hν and Eg were absorption coefficient, a constant related to the effective masses associated with the conduct band and valence band, the absorption energy and band gap energy, respectively; and the parameter n was a pure number corresponding to different electronic transitions (n = 2 or 1/2 for indirect-allowed or direct-allowed transitions, respectively) [37]. The g-C$_3$N$_4$ was reported to be an indirect-allowed semiconductor, i.e., n = 2. Plotting (ahv)^2 versus hν based on the UV–vis DRS spectra in Fig. 2a supported the extrapolated intercept corresponding to Eg values of CN, cCN1, cCN5 and cCN7 composites (Fig. 2b), which were 2.90, 2.85, 2.83 and 2.89 eV, respectively, listed in Table 1. In addition, the UV–vis DRS and the estimated band gap energy of cubic CeO$_2$ were given in Fig. S4. When g-C$_3$N$_4$ hybridized with CeO$_2$, it was deduced that the oxygen atoms in CeO$_2$ might be inevitably doped in the g-C$_3$N$_4$ in the preparation process, leading to the disordered in-plane structural motif of CN, delocalized p-electrons of oxygen atoms and the formation of intermediate energy levels by mixing of N 2p and O 2p orbitals, which would have an influence on the band positions of g-C$_3$N$_4$. XRD results of cCN5 and CN in Fig. S5 further confirmed the speculation. Compared to XRD pattern of pure CN material, the peak at ~13° attributed to CN (100) plane was weakened and broadening on cCN5 sample, suggesting the disorder packing of in-plane structural motif resulted from the doped oxygen atoms in g-C$_3$N$_4$. The similar phenomenon reported by Cui et al. was in O-doped g-C$_3$N$_4$ [38].

It was well-known that the interfacial charge–transfer process played an important role in photocatalytic performances. Therefore, photoluminescence (PL) spectra, as an excellent technique, was used to study the recombination process involved with the interfacial electron-hole pairs between CeO$_2$ nanocube and g-C$_3$N$_4$ sheet [28]. The corresponding spectra were displayed in Fig. S6a. All the samples exhibited a broad PL peak at *ca.* 480 nm with a tail extending to 700 nm. It was previously explained as the down-transfer of the photo-induced charge carriers of g-C$_3$N$_4$ [39]. After introduced CeO$_2$, the PL emission intensity of g-C$_3$N$_4$ was decreased, revealing the faster photoelectron transfer through the hybrid of CeO$_2$ and g-C$_3$N$_4$. It was observed that cCN5 had the lowest PL intensity. Whereas, CeO$_2$ loadings further increased to 7 wt%, the recombination rate of electrons and holes accelerated, which might come from the aggregation of CeO$_2$ and weak interfacial effect. Moreover, the decay of the photoluminescence signals of cCN composites and cCN were tested by time-resolved PL spectra, shown in Fig. S6b. The corresponding PL decay results were listed in Table 1. After grafting the CeO$_2$ nanocubes onto g-C$_3$N$_4$, the decay was prolonged, and cCN5 had the longest PL decay. In short, the interfacial effects on cCN5 efficiently decreased the recombination rate and improved the charge transfer, which could be beneficial for the photoactivity.

To further make sure that cCN5 could improve the photogenerated charge separation and electron transfer process, the photoelectrochemical measurements had been carried out. The transient photocurrent responses of cCN composites and CN were shown in Fig. 3a. A fast and uniform photocurrent response were observed in the as-prepared samples once the light-on and light-off, which implied the extremely fast charge transport. Moreover, it was clear that the loading of CeO$_2$ nanocubes was helpful for the enhanced photocurrent response. Compared with these cCN composites and CN, the cCN5 composite showed the best photocurrent response, which was about 4.5 times higher than that of CN. On the basis of that, it was revealed that the photoinduced charge carriers in the cCN5 composite were separated more efficiently than other cCN composites. To verity this assumption, the elec-

Fig 1. TEM images of (a) CN, (b) cCN1, (c) cCN5, (d) cCN7 composites; and (e) the HRTEM images of the yellow framed area, (f) the enlarged area of the red framed area. (For interpretation of the references to colour in this figure legend, the reader is referred to the web version of this article.)

trochemical impedance spectra (EIS) were also determined, and corresponding results were in Fig. 3b. The semicircles of the Nyquist plots related to cCN composites were reduced compared with CN. Furthermore, cCN5 displayed the shortest semicircle among the three cCN composites, which reflected that the electron transfer process was accelerated in cCN5 [40]. Therefore, on the basis of the above PL and photoelectrochemical results, it was suggested that cCN5 had highly efficient separation of photoinduced electrons and holes, which might result from its more intensive interfacial effects.

3.2. H_2 evolution performance and possible mechanism

The photocatalytic H_2-production activities were evaluated under visible-light ($\lambda \geq 420$ nm) irradiation, with an aqueous solu-

tion containing 10 vol% triethanolamine (TEOA) as a scavenger and 3 wt% Pt as a cocatalyst, in order to reveal the photocatalytic performance of cCN composites and CN composites. In Fig. 4, as could be seen, the cCN composites showed improved photocatalytic activity as compared with pristine CeO_2 and CN, suggesting that the interfacial effects played a key role. The cCN5 composite exhibited the highest H_2 production with 4300 μmol/g after irradiated 5 h, whereas, when the CeO_2 content further increased to 7 wt%, the photocatalytic activity was decreased, probably as a result of more CeO_2 particles blocking the efficient interfacial interaction between CeO_2 and g-C_3N_4. Furthermore, the photoactivity of irregular CeO_2 nanoparticles/g-C_3N_4 with 5 wt% loading (donated as CeCN5 in Fig. 4) was determined. The exposed crystal plane of CeCN5 was {111}, shown in Fig. S7, and the H_2 evolution of CeCN5 was poorer
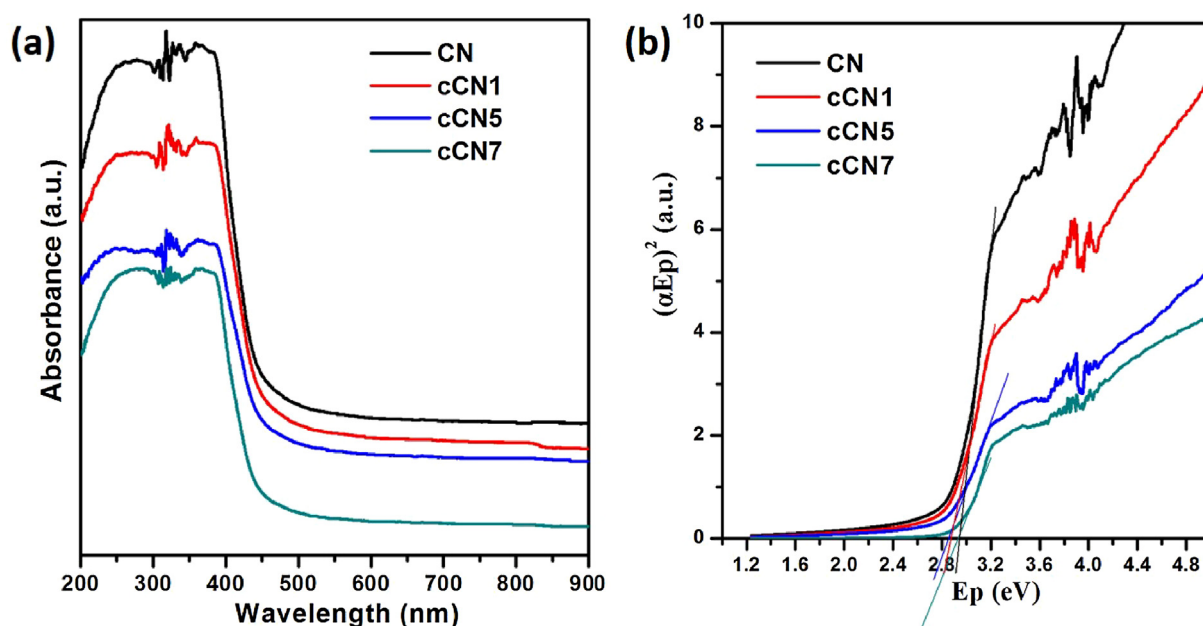
Fig. 2. (a) UV–vis DRS and (b) the estimated band gap energies of cCN composites and CN.
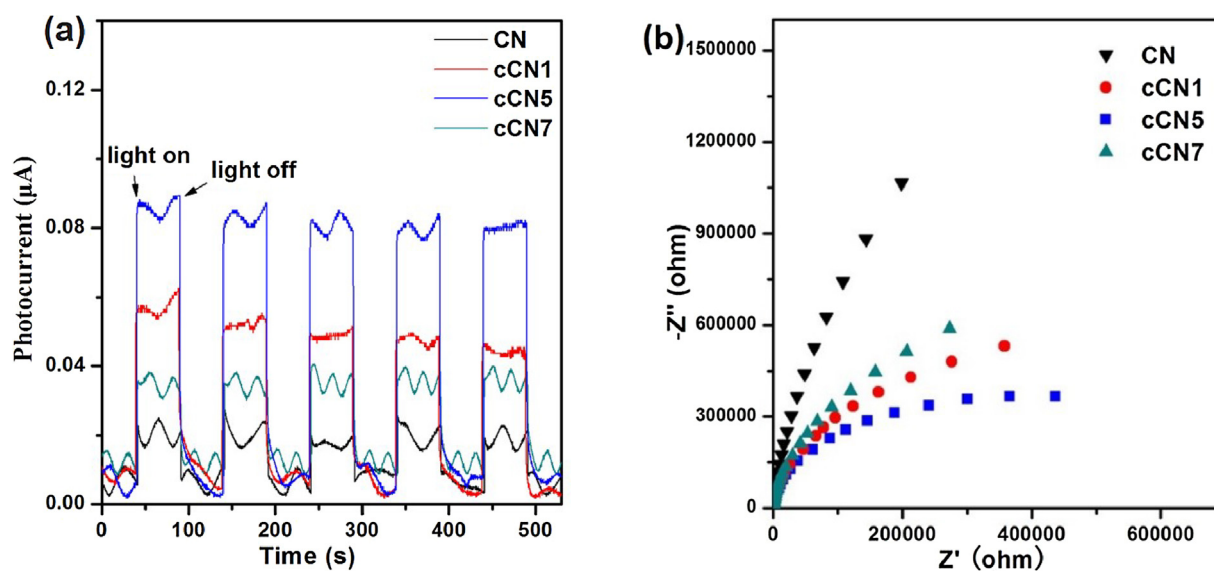

Fig. 3. (a) The transient photocurrent response under visible light irradiation, and (b) EIS spectra of cCN composites and CN.

than that of cCN5. It was reported that holes were encouraged to move toward CeO_2 {100} plane, whereas electrons transferred toward {111} plane under photo-irradiation [25]. On the basis of the above discussion, it was discovered that in the photocatalytic H_2 evolution, the advantageous CeO_2 {100} plane was not only beneficial for the photo-induced electrons transfer to g-C_3N_4, but also enhanced the interfacial interaction between CeO_2 and g-C_3N_4. In order to examine the stability of the obtained cCN composites, the recycling test was performed on cCN5 sample. Fig. S8 showed that there was a slight decrease of H_2 production in 20 h, indicating that the obtained cCN5 possessed good photostability during reaction time.

On the basis of the above discussion, it was suggested that cCN5 composite had the superior photocatalytic activity of H_2 evolution, more visible light adsorption and faster charge transfer, which came from its advantageous interfacial interaction between CeO_2 {100} and g-C_3N_4 sheets. In short, the interfacial effects were of great significance. Therefore, FT-IR and XPS characterizations were introduced to reveal the interfacial effects.

The FT-IR spectra of the various cCN composites and CN were shown in Fig. 5a. The broad peaks between 3600 and 3000 cm^{-1} were attributed to the amino and absorbed hydroxyl groups, and the peaks at ~803, 1235, 1402, 1550, and 1630 cm^{-1} were the typical stretching vibrations of the s-triazine ring system, C=N and C—N heterocycles, respectively [32,33]. Interestingly, from the spectrum of CN, there was a sharp peak at 3582 cm^{-1} ascribed to amino group, while, with the increased loadings of CeO_2 nanocubes, the peak gradually decreased, broadened and shifted to around 3480 cm^{-1}. It was speculated that the adsorbed surface hydroxyl group on cubic CeO_2 {100} planes was hybridized with amino group through the hydrogen bond, leading to the red-shift and broadening. Because it was reported that on CeO_2 {100} planes, there was the coordinated unsaturated ceria atom (Ce_{CUS}), which was facilitated to adsorb OH group [28]. Furthermore, compared with the magnified FT-IR
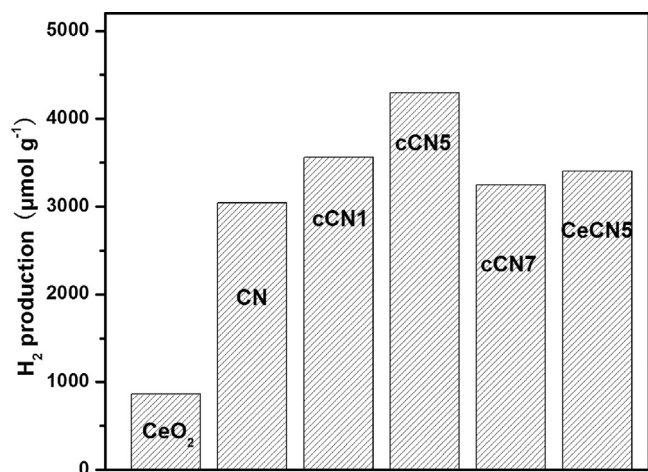
Fig. 4. H$_2$ production of cCN composites, CeO$_2$ and CN under visible light irradiation after 5 h.

spectra (in Fig. 5b), the above mentioned phenomenon was the most obvious in cCN5 sample, suggesting the interaction between CeO$_2$ {100} plane and g-C$_3$N$_4$ was the most intensive, leading to its enhanced photocatalytic performance and charge transfer process.

The interfacial electronic states of cCN composites and CN were further measured by XPS characterization to show the interfacial interactions. The XPS spectra of N 1s and C 1s for the cCN composites and CN were provided in Fig. 6a and b. According to literatures, the N 1s spectra in Fig. 6a could be fitted into four peaks. The peaks centered at *ca.* 398.5 and 399.7 eV were attributed to sp^2-hybridized nitrogen atom (C=N—C group) and tertiary nitrogen (N—C$_3$ group or H—N—C$_2$), respectively. The peaks at *ca.* 401.0 and 404.2 eV derived from amino function groups and charging effect localization in heterocycles, respectively [41,42]. As for C 1s spectra in Fig. 6b, the peak at *ca.* 284.6 eV was assigned to carbon contamination, and the peak at *ca.* 287.8 eV was related to the sp^2-bonded carbon atom (N—C=N) of g-C$_3$N$_4$ in aromatic rings [27,28]. Interesting, it was obvious that the binding energies of N 1s and C 1s peaks, ascribed to sp^2-bonded nitrogen and carbon atoms in s-triazine ring, showed

lower value in cCN5 composite (shown in Table S1), suggesting that more electrons donated to the π ring of the s-triazine (g-C$_3$N$_4$). It was considered that the electron transfer resulted from the interfacial effects via the p-electron of O$_{CUS}$ atom (CeO$_2$ {100}) donation to the π ring of the s-triazine (g-C$_3$N$_4$), which was similar with the previous reports [43,44]. From the inserted figures (in Fig. 6a and b), it was found that the peak shift of cCN5 composite was more obvious from the stronger interaction.

In addition, the high-resolution XPS spectra of O 1s and Ce 3d were displayed in Fig. 6c, d. For the spectra of O 1s (Fig. 6c), the peaks labeled as O′ (*ca.* 528.5 eV) was attributed to the lattice oxygen in CeO$_2$, and a broad peak centered at *ca.* 532.0 eV labeled as O″ was the adsorbed oxygen (*e.g.* oxygen in hydroxyl groups) [21,32]. With the increased loadings of CeO$_2$, of course, the signal of lattice oxygen became larger. Interestingly, the peak of adsorbed oxygen displayed a broad feature. The broad peak came from the change of electronic state of adsorbed oxygen species, which were attributed to chemisorbed H$_2$O (donated as O″$_\beta$) and adsorbed OH groups (donated as O″$_\alpha$), respectively [45,46]. When the CeO$_2$ nanocubes were loading, the peak position of the adsorbed OH groups O″$_\alpha$ shifted to the lower binding energy, which indicated that the electrons on oxygen atoms of OH groups increased. Combined with the FT-IR result, the formed hydrogen bond was the key factor. Because oxygen atom had stronger electronegativity than that of nitrogen atom, leading to more electrons transfer to oxygen atom via hydrogen bond, and then the XPS peak of adsorbed OH groups shifted to lower binding energy. Therefore, CeO$_2$ loading increased the amount of interfacial hybridized hydroxyl group, and then enhanced the interfacial interactions. The intensive interfacial effect was more obvious in cCN5 sample, in agreement with the FT-IR results.

Furthermore, the Ce 3d spectra of these samples were investigated. The peak in Fig. 6d was fitted into eight peaks labeled as u′ and v′ to Ce^{3+}, and the other six peaks labeled as u‴, u″, u, v‴, v″ and v to Ce^{4+} [21,24]. The content ratio of Ce^{3+} to Ce^{4+} over cCN composites were calculated in Table 1. It was clearly that the Ce^{3+} content in cCN5 was higher than that of cCN1 and cCN7 samples. It had been reported that water was more inclined to be adsorbed
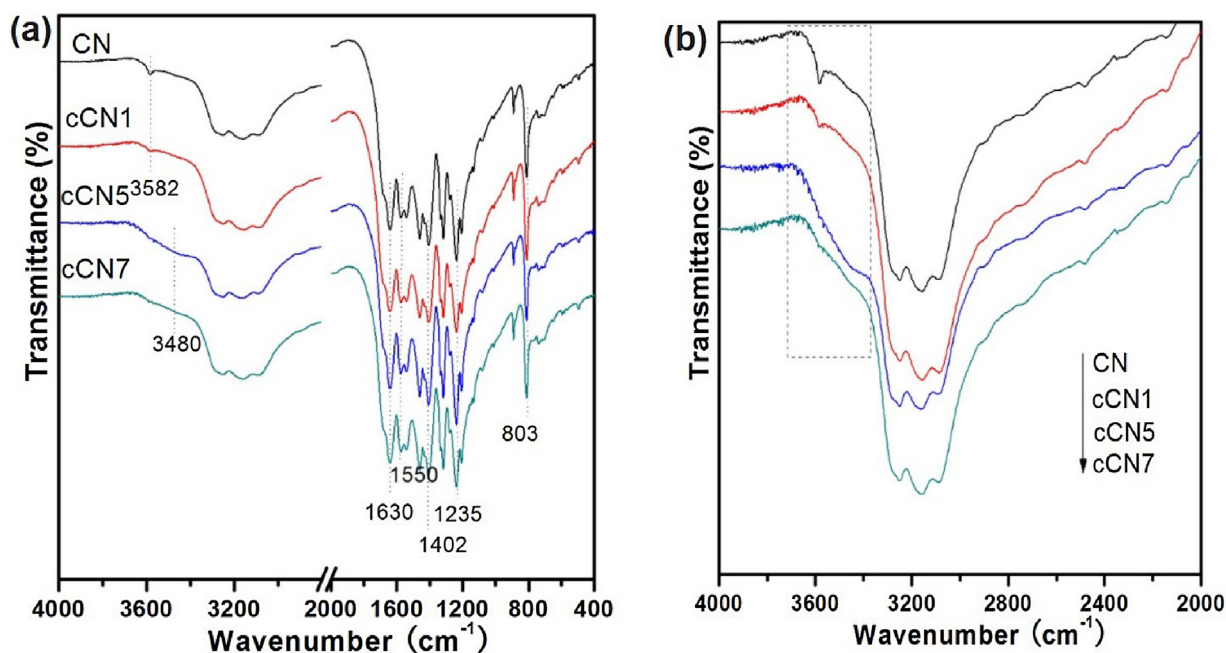

Fig. 5. (a) FT-IR results and (b) the magnified graph of cCN composites and CN.
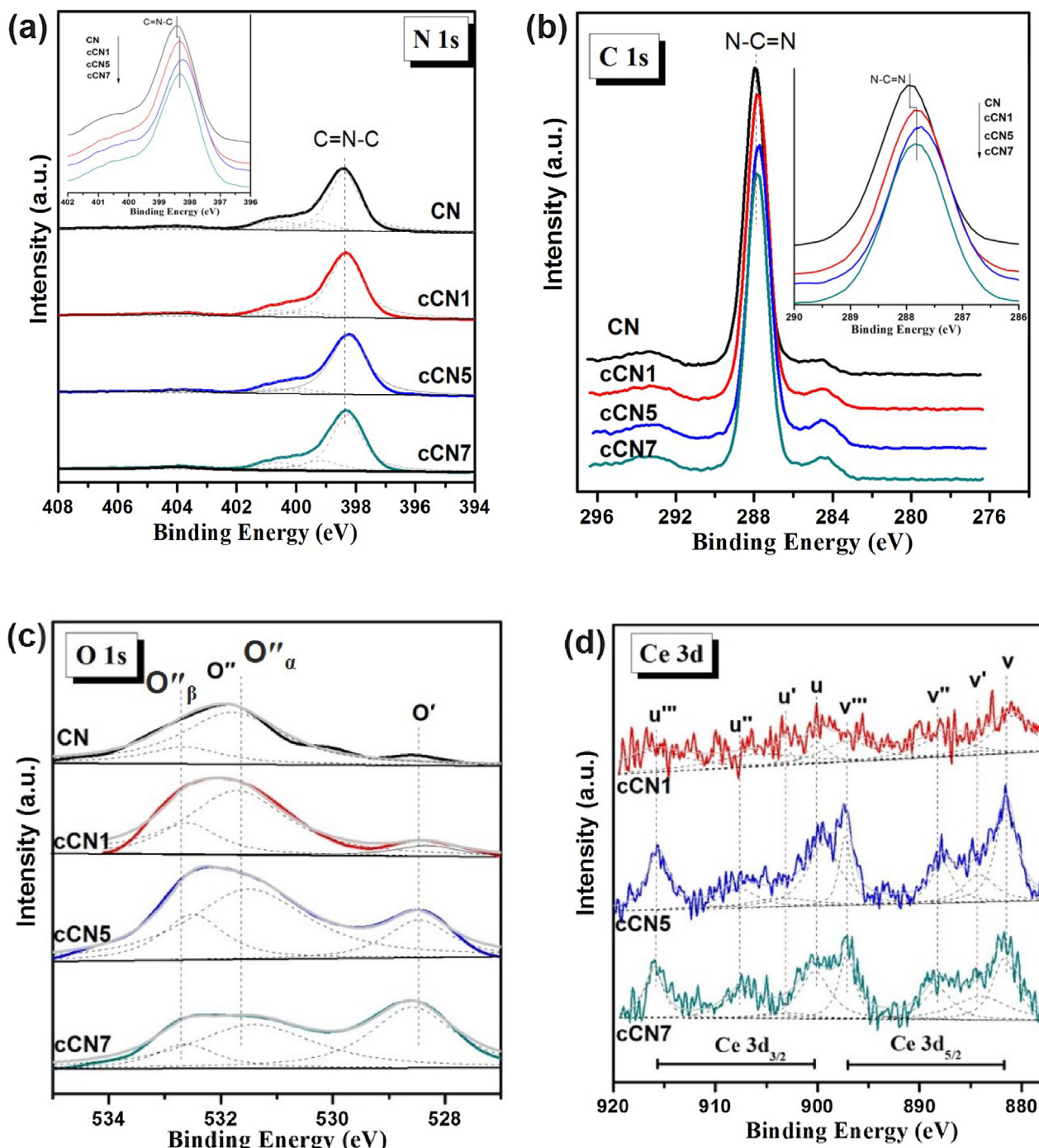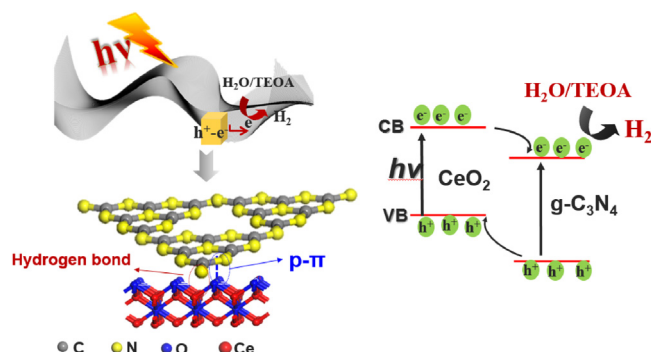
Fig. 6. XPS spectra of (a) N 1s, (b) C 1s regions (the magnified graphs were inserted), (c) O 1s and (d) Ce 3d of cCN composites and CN.

on Ce^{3+} than that on Ce^{4+} species [47], which was helpful for water reduction.

The *in-situ* ESR spin-trap technique was determined, in order to further confirm the faster interfacial photo-excited electron transfer in cCN5 composite (in Fig. S9). The signals of generated $^{\bullet}O_2{}^{-}$ radicals on cCN5 were more intensive than that of CN sample, which indicated more interfacial transferred electrons on cCN5 composite could be efficiently captured, due to the advantageous interfacial effects.

On the basis of the above photocatalytic performances and characterizations, it was suggested that the interfacial effect between CeO_2 {100} crystal plane and g-C_3N_4 sheet played an important role, which exerted an influence on the light-absorption and the recombination rates of photo-generated electrons and holes. The cCN5 composite had the advantageous interfacial effect, which was the best for the effectively photoreduction of water. Therefore, on the basis of FT-IR and XPS results, the possible schematic illustration of the interfaces between CeO_2 {100} crystal plane and g-C_3N_4 sheet was proposed. In Fig. 7, the coordinated unsaturated O (O_{CUS}) and ceria (Ce_{CUS}) existed on interface between CeO_2 {100} and g-C_3N_4 sheets. Generally, O_{CUS} was more active with p electron, leading to the stronger interfacial contact with g-C_3N_4 sheet by p-π effect. Moreover, the hydroxyl group was beneficial for adsorption on Ce_{CUS}, which could connect with amino group of g-C_3N_4 by

Fig. 7. Schematic illustrations of the proposed interaction in the c-CeO$_2$/g-C$_3$N$_4$ interface and the diagram of electron–hole pair separation and the possible reaction mechanism.

hydrogen bond. With the increased loadings of CeO$_2$, the interfacial effect would be enhanced, while, when the loading was over 5 wt%, the above interfacial connection would be blocked by the assembled CeO$_2$ nanocubes. Therefore, cCN5 composite displayed the superior photocatalytic performances. Furthermore, the diagram of electron–hole pair separation and the possible reaction mechanism were also described, based on the previous UV–vis DRS and XPS valence band results. Under the visible light irradiation, the photoinduced electrons were transferred to the conduction band (CB) of CeO$_2$. For their energy band bending in space charge region, subsequently, the photogenerated electrons in CeO$_2$ would migrate to the CB of g-C$_3$N$_4$, and then the adsorbed water/TEOA was reduced to H$_2$. Meantime, the holes in g-C$_3$N$_4$ transferred to VB of CeO$_2$.

4. Conclusions

In summary, with 5 wt% c-CeO$_2$ loading, the c-CeO$_2$/g-C$_3$N$_4$ composite exhibited more visible light adsorption, faster charge transfer and the superior photocatalytic hydrogen evolution under visible light, which resulted from the interfacial effects. The advantageous CeO$_2$ {100} plane was not only enhanced the interfacial interaction between CeO$_2$ and g-C$_3$N$_4$ via the hydrogen bond and p-π hybrid, but also beneficial for the photo-induced electrons transferring to g-C$_3$N$_4$. The work disclosed that the interfacial effects, which was the key factor for photocatalysis.

Acknowledgements

Appendix A. Supplementary data

Supplementary data associated with this article can be found, in the online version, at http://dx.doi.org/10.1016/j.apcatb.2017.03.085.

References

[1] S. Chu, A. Majumdar, Opportunities and challenges for a sustainable energy future, Nature 488 (488) (2012) 294–303.

[2] Q. Xiang, J. Yu, M. Jaroniec, Graphene-Based semiconductor photocatalysts, Chem. Soc. Rev. 41 (2012) 782–796.

[3] Z.F. Bian, F.L. Cao, J. Zhu, H.X. Li, Plant uptake-assisted round-the-clock photocatalysis for complete purification of aquaculture wastewater using sunlight, Environ. Sci. Technol. 49 (2015) 2418–2424.

[4] H. Tong, S.X. Ouyang, Y.P. Bi, N. Umezawa, M. Oshikiri, J.H. Ye, Nano-photocatalytic materials: possibilities and challenges, Adv. Mater. 24 (2012) 229–251.

[5] Z.F. Bian, J. Zhu, H.X. Li, Solvothermal alcoholysis synthesis of hierarchical TiO$_2$ with enhanced activity in environmental and energy photocatalysis, J. Photochem. Photobiol. C 28 (2016) 72–86.

[6] A. Fujishima, K. Honda, Electrochemical photolysis of water at a semiconductor electrode, Nature 238 (1972) 37–38.

[7] X.B. Chen, S.H. Shen, L.J. Guo, S.S. Mao, Semiconductor based photocatalytic hydrogen generation, Chem. Rev. 110 (2010) 6503–6570.

[8] C. Tang, L.F. Liu, Y.L. Li, Z.F. Bian, Aerosol spray assisted assembly of TiO$_2$ mesocrystals into hierarchical hollow microspheres with enhanced photocatalytic performance, Appl. Catal. B: Environ. 201 (2017) 41–47.

[9] A. Kudo, Y. Miseki, Heterogeneous photocatalyst materials for water splitting, Chem. Soc. Rev. 38 (2009) 253–278.

[10] F.L. Cao, Y.L. Li, C. Tang, X.F. Qian, Z.F. Bian, Fast synthesis of anatase TiO$_2$ single crystals by a facile solid-state method, Res. Chem. Intermed. 42 (2016) 5975–5981.

[11] Y. Shiraishi, S. Kanazawa, Y. Sugano, D. Tsukamoto, H. Sakamoto, S. Ichikawa, T. Hirai, Highly selective production of hydrogen peroxide on graphitic carbon nitride (g-C$_3$N$_4$) photocatalyst activated by visible light, ACS Catal. 4 (2014) 774–780.

[12] D.M. Chen, K.W. Wang, W.Z. Hong, R.L. Zong, W.Q. Yao, Y.F. Zhu, Visible light photoactivity enhancement via CuTCPP hybridized g-C$_3$N$_4$ nanocomposite, Appl. Catal. B: Environ. 166–167 (2015) 366–373.

[13] S.W. Cao, J.G. Yu, G-C$_3$N$_4$-Based photocatalysts for hydrogen generation, J. Phys. Chem. Lett. 5 (2014) 2101–2107.

[14] L. Zhang, D.W. Jing, X.L. She, H.W. Liu, D.J. Yang, Y. Lu, J. Li, Z.F. Zheng, L.J. Guo, Heterojunctions in g-C$_3$N$_4$/TiO$_2$(B) nanofibres with exposed (001) plane and enhanced visible-light photoactivity, J. Mater. Chem. A 2 (2014) 2071–2078.

[15] M. Zhang, X.J. Bai, D. Liu, J. Wang, Y.F. Zhu, Enhanced catalytic activity of potassium-doped graphitic carbon nitride induced by lower valence position, Appl. Catal. B: Environ. 164 (2015) 77–81.

[16] Q. Xiang, J. Yu, M. Jaroniec, Preparation and enhanced visible light photocatalytic H$_2$-Production activity of Graphene/C$_3$N$_4$ composites, J. Phys. Chem. C 115 (2011) 7355–7363.

[17] D.L. Jiang, J. Li, C.S. Xing, Z.Y. Zhang, S.C. Meng, M. Chen, ACS Appl. Mater. Interfaces 7 (2015) 19234–19242.

[18] D.M. Chen, K.W. Wang, T.Z. Ren, H. Ding, Y.F. Zhu, Synthesis and characterization of the ZnO/mpg-C$_3$N$_4$ heterojunction photocatalyst with enhanced visible light photoactivity, Dalton Trans. 43 (2014) 13105–13114.

[19] X.R. Li, J.G. Wang, Y. Men, Z.F. Bian, TiO$_2$ mesocrystal with exposed (001) facets and CdS quantum dots as an active visible photocatalyst for selective oxidation reactions, Appl. Catal. B: Environ. 187 (2016) 115–121.

[20] F.F. Chen, F.L. Cao, H.X. Li, Z.F. Bian, Exploring the important role of nanocrystals orientation in TiO$_2$ superstructure on photocatalytic performances, Langmuir 31 (2015) 3494–3499.

[21] T. Shido, Y. Iwasawa, Regulation of reaction intermediate by reactant in the water-gas shift reaction on CeO$_2$, in relation to reactant-promoted mechanism, J. Catal. 136 (1992) 493–503.

[22] X.J. Yao, Y. Xiong, W.X. Zou, L. Zhang, S.H. Wu, X. Dong, F. Gao, Y. Deng, C.J. Tang, Z. Chen, L. Dong, Y. Chen, Correlation between the physicochemical properties and catalytic performances of CexSn$_{1-x}$O$_2$ mixed oxides for NO reduction by CO, Appl. Catal. B: Environ. 144 (2014) 152–165.

[23] P. Jasinski, T. Suzuki, H.U. Anderson, Nanocrystalline undoped ceria oxygen sensor, Sens. Actuators B 95 (2003) 73–77.

[24] L. Qi, Qi. Yu, Y. Dai, C.J. Tang, L.J. Liu, H.L. Zhang, F. Gao, L. Dong, Y. Chen, Influence of cerium precursors on the structure and reducibility of mesoporous CuO-CeO$_2$ catalysts for CO oxidation, Appl. Catal. B: Environ. 119–120 (2012) 308–320.

[25] P. Li, Y. Zhou, Z.Y. Zhao, Q.F. Xu, X.Y. Wang, M. Xiao, Z.G. Zou, Hexahedron prism-anchored octahedronal CeO$_2$: crystal facet based homojunction promoting efficient solar fuel synthesis, J. Am. Chem. Soc. 137 (2015) 9547–9550.

[26] W.Y. Lei, T.T. Zhang, L. Gu, P. Liu, Joseí A. Rodriguez, G. Liu, M.H. Liu, Surface-Structure sensitivity of CeO$_2$ nanocrystals in photocatalysis and enhancing the reactivity with nanogold, ACS Catal. 5 (2015) 4385–4393.

[27] M. Li, Z. Wu, S.H. Overbury, Surface structure dependence of selective oxidation of ethanol on faceted CeO$_2$ nanocrystals, J. Catal. 306 (2013) 164–176.

[28] W.X. Zou, C.Y. Ge, M.Y. Lu, S.G. Wu, Y.Z. Wang, J.F. Sun, Y. Pu, C.J. Tang, F. Gao, L. Dong, Engineering the NiO/CeO$_2$ interface to enhance the catalytic performance for CO oxidation, RSC Adv. 5 (2015) 98335–98343.

[29] R. Verma, S.K. Samdarshi, In situ decorated optimized CeO$_2$ on reduced graphene oxide with enhanced adsorptivity and visible light photocatalytic stability and reusability, J. Phys. Chem. C 120 (2016) 22281–22290.

[30] S.C. Hu, F. Zhou, L.Z. Wang, J.L. Zhang, Preparation of Cu$_2$O/CeO$_2$ heterojunction photocatalyst for the degradation of Acid Orange 7 under visible light irradiation, Catal. Commun. 12 (2011) 794–797.

[31] L. Wang, J. Ding, Y.Y. Chai, CeO$_2$ nanorod/g-C$_3$N$_4$/N-rGO composite: enhanced visible-light-driven photocatalytic performance and the role of N-rGO as electronic transfer media, Dalton Trans. 44 (2015) 7021–7031.

[32] X.J. She, H. Xu, H.F. Wang, J.X. Xia, Y.H. Song, J. Yan, Y.G. Xu, Q. Zhang, D.L. Du, H.M. Li, Controllable synthesis of CeO$_2$/g-C$_3$N$_4$ composites and their applications in the environment, Dalton Trans. 44 (2015) 7021–7031.

[33] M.L. Li, L.X. Zhang, M.Y. Wu, Y.Y. Du, X.Q. Fan, M. Wang, L.L. Zhang, Q.L. Kong, J.L. Shi, Mesostructured CeO$_2$/g-C$_3$N$_4$ nanocomposites: remarkably enhanced photocatalytic activity for CO$_2$ reduction, Nano Energy 19 (2016) 145–155.

[34] N. Tian, H.W. Huang, C.Y. Liu, F. Dong, T.R. Zhang, X. Du, S.X. Yu, Y.H. Zhang, In situ co-pyrolysis fabrication of CeO_2/g-C_3N_4 n–n type heterojunction for synchronously promoting photo-induced oxidation and reduction properties, J. Mater. Chem. A 3 (2015) 17120–17130.

[35] C.S. Pan, J. Xu, Y.J. Wang, D. Li, Y.F. Zhu, Dramatic activity of C_3N_4/$BiPO_4$ photocatalyst with core-shell structure formed by self-assembly, Adv. Funct. Mater. 22 (2012) 1518–1524.

[36] X.F. Yang, Z.P. Chen, J.S. Xu, H. Tang, K.M. Chen, Y. Jiang, Tuning the morphology of g-C_3N_4 for improvement of Z-Scheme photocatalytic water oxidation, ACS Appl. Mater. Interfaces 7 (2015) 15285–15293.

[37] H.W. Huang, Y. He, Z.S. Lin, L. Kang, Y.H. Zhang, Two novel Bi-based borate photocatalysts: crystal structure, electronic structure, photoelectrochemical properties, and photocatalytic activity under simulated solar light irradiation, J. Phys. Chem. C 117 (2013) 22986–22994.

[38] Y.X. Wang, H. Wang, F.Y. Chen, F. Cao, X.H. Zhao, S.G. Meng, Y.J. Cui, Facile synthesis of oxygen doped carbon nitride hollow microsphere for photocatalysis, Appl. Catal. B: Environ. 206 (2017) 417–425.

[39] X. Wang, S. Blechert, M. Antonietti, Polymeric graphitic carbon nitride for heterogeneous photocatalysis, ACS Catal. 2 (2012) 1596–1606.

[40] B. Hu, F.P. Cai, T.J. Chen, M.S. Fan, C.J. Song, X. Yan, W.D. Shi, Hydrothermal synthesis g-C_3N_4/Nano-$InVO_4$ nanocomposites and enhanced photocatalytic activity for hydrogen production under visible light irradiation, ACS Appl. Mater. Interfaces 7 (2015) 18247–18256.

[41] D. Gao, Q. Xu, J. Zhang, Z. Yang, M. Si, Z. Yan, D. Xue, Defect-related ferromagnetism in ultrathin metal-free g-C_3N_4 nanosheets, Nanoscale 6 (2014) 2577–2581.

[42] S. Wang, C. Li, T. Wang, P. Zhang, A. Li, J. Gong, Controllable synthesis of nanotube-type graphitic C_3N_4 and their visible-light photocatalytic and fluorescent properties, J. Mater. Chem. A 2 (2014) 2885–2890.

[43] X.J. Bai, L. Wang, Y.J. Wang, W.Q. Yao, Y.F. Zhu, Enhanced oxidation ability of g-C_3N_4 photocatalyst via C_{60} modification, Appl. Catal. B: Environ. 152–153 (2014) 262–270.

[44] W.X. Zou, L. Zhang, L.C. Liu, X.B. Wang, J.F. Sun, S.G. Wu, Y. Deng, C.J. Tang, F. Gao, L. Dong, Engineering the Cu_2O–reduced graphene oxide interface to enhance photocatalytic degradation of organic pollutants under visible light, Appl. Catal. B: Environ. 181 (2016) 495–503.

[45] K. Tabata, Y. Hirano, E. Suzuki, XPS studies on the oxygen species of $LaMn_{1-x}Cu_xO_{3+\lambda}$, Appl. Catal. A: Gen. 170 (1998) 245–254.

[46] J. Carrasco, D. López-Durán, Z.Y. Liu, T. Duchoň, J. Evans, S.D. Senanayake, E.J. Crumlin, V. Matolín, J.A. Rodríguez, M.V. Ganduglia-Pirovano, In situ and theoretical studies for the dissociation of water on an active Ni/CeO_2 catalyst: importance of strong metal–support interactions for the cleavage of O—H bonds, Angew. Chem. Int. Ed. 54 (2015) 1–6.

[47] R.K. Pati, I.C. Lee, S. Hou, O. Akhuemonkhan, K.J. Gaskell, Q. Wang, A.I. Frenkel, D. Chu, L.G. Salamanca-Riba, S.H. Ehrman, Flame synthesis of nanosized Cu-Ce-O Ni-Ce-O, and Fe-Ce-O catalysts for the water-gas shift (WGS) reaction, ACS Appl. Mater. Interfaces 1 (2009) 2624–2635.